Asteroseismology of the Ancient Naked-Eye Exoplanet Host Star ν^2 Lupi

Angharad Weeks[1,2,⋆] Daniel Huber[2,3], Amalie Stokholm[4], Martin Bo Nielsen[4], Yaguang Li[3], Vincent Van Eylen[1], Timothy R. Bedding[2], J. M. Joel Ong[3,5], Christopher J. Lindsay[6],
[1]*Mullard Space Science Laboratory, University College London, Dorking, Surrey, RH5 6NT*
[2]*Sydney Institute for Astronomy, School of Physics, University of Sydney NSW 2006, Australia*
[3]*Institute for Astronomy, University of Hawai'i, 2680 Woodlawn Drive, Honolulu, HI 96822, USA*
[4]*School of Physics and Astronomy, University of Birmingham, Edgbaston, Birmingham, B15 2TT,United Kingdom*
[5]*NASA Hubble Fellow*
[6]*Department of Astronomy, Yale University, P.O. Box 208101, New Haven, CT 06520-8101, USA*

Accepted XXX. Received YYY; in original form ZZZ

ABSTRACT

High-precision lightcurves from space-based telescopes and precise astrometry from the Gaia satellite have revolutionised our ability to characterise exoplanet host stars. Asteroseismology has allowed for stellar parameters to be determined to remarkable precision, achieving age uncertainties as low as 10-20% for Sun-like dwarfs. We present an asteroseismic analysis of the naked-eye (V = 5.65) star ν^2 Lupi (HD 136352), which hosts three small transiting planets with orbital periods of 11, 27, and 107 days. We used the latest 20-second cadence photometry data from the Transiting Exoplanet Survey Satellite (TESS) to extract stellar oscillations. Comparing these to stellar models, we find that the star has a mass of $0.829^{+0.038}_{-0.030}$ (ran) ±0.03 (sys) $M_\odot$, a radius of $1.00^{+0.013}_{-0.017}$ (ran) ±0.04 (sys) $R_\odot$ and an age of $11.9^{+2.6}_{-1.6}$ (ran) ±1.7 (sys) Gyr. We also confirm that the star is likely a member of the Galactic thick disk based on its Galactic velocities, consistent with the asteroseismic age. Based on the newly determined stellar parameters, we recalculate the planet parameters. The inner planet has a mass of 4.55 ± 0.40 $M_\oplus$ and a radius of 1.57 ± 0.038 $R_\oplus$, suggesting the planet is rocky and consisting primarily of silicates without an iron-rich core, consistent with its old age and significant alpha-element enhancement. The two outer planets have masses and radii of 10.87 ± 0.62 $M_\oplus$ and 2.75 ± 0.064 $R_\oplus$, and 8.52 ± 0.90 $M_\oplus$ and 2.42 ± 0.077 $R_\oplus$, respectively, suggesting both are sub-Neptune planets with a significant H-He atmosphere.

Key words: – Asteroseismology – planets and satellites: terrestrial planets – planets and satellites: fundamental parameters – stars: low-mass

1 INTRODUCTION

Accurate characterisation of exoplanet host stars is vital for our understanding of the properties of exoplanets. This applies to individual systems, because planet properties are often measured indirectly and relative to their host star properties. It also applies to planet population studies, where linking the statistical properties of exoplanet populations to stellar parameters can constrain how planets form.

This can be achieved by measuring the occurrence of planets as a function of stellar parameters, such as $T_{\rm eff}$ (Howard et al. 2012), evolutionary state (Grunblatt et al. 2019), stellar type (Bryant et al. 2023; Ment & Charbonneau 2023; Gan et al. 2023), metallicity (Gonzalez 1997; Fischer & Valenti 2005; Boley et al. 2024), or age (Miyazaki & Masuda 2023; Sayeed et al. 2025). This can also be probed by comparing the characteristics of close-in planets, such as planet compositions (Adibekyan et al. 2021; Weeks et al. 2024), or radii (Chen et al. 2023; Ho et al. 2024) to the properties of their host stars.

For many host stars, stellar parameters can now be precisely determined using high-quality photometric, spectroscopic, and astrometric observations, including those made by Gaia (Gaia Collaboration et al. 2016). Stellar radii in particular are precisely known. This is true for individual host stars (see e.g. Dai et al. 2023; DiTomasso et al. 2025, for recent examples), in addition to larger, homogeneous samples (e.g. Stassun et al. 2019; Berger et al. 2020; Magrini et al. 2022; Bonomo et al. 2023; Swastik et al. 2023; Tsantaki et al. 2025). However, other stellar parameters, in particular stellar ages, remain challenging to determine because sun-like stars evolve slowly on the main sequence. Asteroseismology resolves this issue by probing the core properties, which evolve much more quickly over a star's lifetime. This method relies on the study of stellar oscillations whose frequencies are determined by the inner physical characteristics of a star (Bedding & Kjeldsen 2003; Aerts et al. 2010; Kjeldsen & Bedding 2011). As a result of this unique sensitivity to the stellar interior, asteroseismology offers the most precise constraints on stellar properties (Lebreton et al. 2014; García & Ballot 2019).

Stars exhibiting solar-like oscillations, which are excited by convection in the envelope (Chaplin & Miglio 2013; Bedding 2014; Basu 2016), can been studied to high precision using Asteroseismology. This method has been successfully applied to exoplanet host stars, which has enabled tighter photometric constraints on exoplanet sci-

⋆ E-mail: angharad.weeks.20@ucl.ac.uk

ence cases, (see e.g., Lundkvist et al. 2018, for a review). However, asteroseismology has been successfully applied to only around 5% of planet host stars, and such high-quality observations are rare. As a result, the method has largely been limited to relatively bright exoplanet host stars observed by *Kepler* (e.g., Huber et al. 2013a; Lund et al. 2014; Lundkvist et al. 2016; Kayhan et al. 2019). Additionally, many of these planet host stars only have measurable global seismic properties (the frequency of maximum power, $\nu_{\rm max}$, and the frequency separation, $\Delta\nu$). Via well established scaling relations (Kjeldsen & Bedding 1995; Guggenberger et al. 2016), these global parameters allow determination of stellar mass and radius (e.g. Yıldız et al. 2019), but not of stellar age. Where available, measurements of individual mode frequencies enable determination of mass and radius a to a precision of few percent, and 10–20 % for stellar age (Bruntt 2009; Chaplin et al. 2011, 2014; Lebreton et al. 2014). The identification of these frequencies has been possible only for the best-observed cases of planet hosting solar-like oscillators (e.g., Huber et al. 2013b; Silva Aguirre et al. 2015; Davies et al. 2016; Lundkvist et al. 2016).

Beyond *Kepler*, asteroseismology has been successfully applied to a number of stars with time series from the *TESS* satellite (Ricker et al. 2015). This includes exoplanet host stars analysed via modelling of individual frequencies such as π Men (Huber et al. 2022), HD 221416 (Huber et al. 2019), γ^2 For (Nielsen et al. 2020), HD 212771 and HD 203949 (Campante et al. 2019), and HD 76920 (Jiang et al. 2023). However, the Nyquist frequency of the nominal *TESS* mission observations for most stars was 278 μHz, which limited asteroseismic detections with these data to those in more evolved stars. A select sample of only 20,000 stars were observed with a dedicated 120-second cadence mode, providing data with a Nyquist frequency of 4167 μHz, Therefore, solar-like oscillation frequencies have only been detected two main-sequence host stars with $\log g > 3.5$ observed with *TESS*, namely π Men and γ^2 For.

In its extended mission, *TESS* is now re-observing a number of targets at a 20-second observing cadence. This provides improved photometric precision for bright ($V_T > 8$) stars, and increases the Nyquist frequency to 25000 μHz, allowing the detection of oscillations in more Sun-like planet hosts (Huber et al. 2022).

In this paper we present the discovery of solar-like oscillations in ν^2 Lupi using *TESS*. Three small (1.5-3 $R_\oplus$) planets were initially discovered orbiting this star, via the radial velocity (RV) method by Udry et al. (2019). Subsequently, two of these planets, with periods of 11 and 27 days, were observed to transit using *TESS* photometry (Kane et al. 2020). The third planet, with a period of 107 days, was later also seen to transit using dedicated *CHEOPS* observations (Delrez et al. 2021). ν^2 Lupi is one of the brightest stars with transiting planets, and is a prime target for the detection of further companions (see e.g. Udry et al. 2019) or exomoons (Ehrenreich et al. 2023). The planets orbiting ν^2 Lupi also provide an excellent opportunity to study the exoplanet radius valley, a dearth of exoplanets at around 1.8 $R_\oplus$ (Fulton et al. 2017; Van Eylen et al. 2018). This valley separates super-Earth planets with stripped atmospheres from sub-Neptune planets, with extended gaseous envelopes, likely consisting of primarily Hydrogen and Helium (Bean et al. 2021). The formation of this valley has been attributed atmospheric mass loss, which may be due to stellar radiation (e.g., Owen & Wu 2013, 2017; Owen 2019; Cloutier & Menou 2020). However, this atmospheric mass loss may alternatively be due to the internal heat of the planet itself (e.g. Ginzburg et al. 2018; Gupta & Schlichting 2019, 2020). A precise age of the ν^2 Lupi system is particularly useful, as different radius valley mechanisms are predicted to act over vastly different timescales (see e.g., Venturini et al. 2020; Rogers & Owen 2021; David et al. 2021). Having planets below and above the valley, this system is a unique testbed to probe radius valley formation theories.

In this work we use *TESS* 20-second cadence observations to extract individual oscillation frequencies. We combine these with spectroscopic, photometric, and astrometric constraints to perform a state-of-the-art asteroseismic analysis of ν^2 Lupi and constrain its stellar properties, including age. We then use these stellar properties to recalculate planet properties, and investigate the nature of this exciting planetary system. ν^2 Lupi is the oldest, brightest and closest planet-hosting dwarf with *TESS* asteroseismology.

Table 1. Spectroscopic parameters of ν^2 Lupi. The temperature from Kane et al. (2020) was determined using photometry. * indicates [M/H], as opposed to [Fe/H]

Source	$T_{\rm eff}$ [K]	[Fe/H]	$\log g$
Delrez et al. (2021)	5664 ± 61	-0.34 ± 0.04	4.39 ± 0.11
Kane et al. (2020)	5850 ± 100	-0.25 ± 0.12	$4.39^{+0.03}_{-0.03}$
Stassun et al. (2019)	5739^{+109}_{-112}	-0.26 ± 0.01*	$4.43^{+0.07}_{-0.08}$
Sousa et al. (2008)	5664 ± 14	-0.34 ± 0.01	4.38 ± 0.02

2 DATA ANALYSIS

2.1 TESS Photometry

ν^2 Lupi was observed in 20-second cadence data mode in sectors 38 and 65 of the *TESS* mission. We used the SPOC (TESS Science Processing Operations Center) light curves (Jenkins et al. 2016) from these sectors, excluded data points more than 5σ away from the median, and removed data affected by instrumental effects in the final 4 days of sector 65. We masked out the seven transits present in the data, using the transit period, transit duration, and epoch, from the TOI list (Guerrero et al. 2021) as shown in Fig. 1. We also excluded any data with non-zero quality flags from SPOC.

2.2 Spectroscopy

ν^2 Lupi is a bright target ($m_V = 5.78$), and therefore has been extensively studied with photometric and spectroscopic surveys. We list the most recent spectroscopic and photometric measurements in Table 1. We adopt the most recent parameters from Delrez et al. (2021) for our analysis. In order to account for systematic errors that result from determination of parameters using different methodologies in the literature, we take the standard deviation of literature reported values and add this range in quadrature to the reported uncertainty values from Delrez et al. (2021). The resulting spectroscopic values are $T_{\rm eff} = 5664 \pm 130$ K and [Fe/H] $= -0.34 \pm 0.08$.

2.3 Photometry

We calculated the luminosity from the Johnson V magnitude m_V and the parallax ϖ from *Gaia* DR3 (Gaia Collaboration et al. 2016, 2021), using `isoclassify` (Huber et al. 2017; Berger et al. 2020, 2023). We find a value of $L_\star = 1.00 \pm 0.04$ $L_\odot$, which is in excellent agreement with the value calculated by Delrez et al. (2021); $L_\star = 1.038 \pm 0.059$ $L_\odot$.

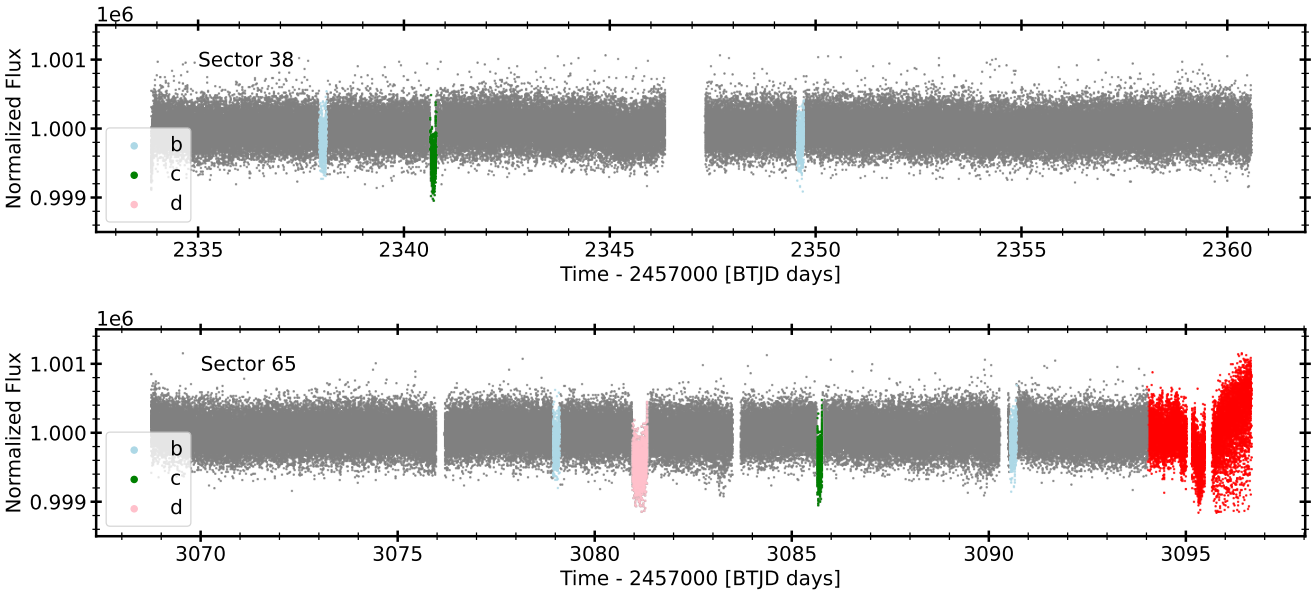

Figure 1. 20-second cadence light curve for ν^2 Lupi from the Transiting Exoplanet Survey Satellite. Transit masks for planets b, c and d are shown in blue, green, and pink respectively. Data removed from the light curve due to instrumental effects are shown in red. The grey remaining points show data with 5σ outliers removed, and with a 1-day flattening function applied.

Table 2. Input parameters of ν^2 Lupi. Sources : 1 - Gaia Collaboration et al. (2016), 2 - Abazajian et al. (2009), 3 - Delrez et al. (2021)

Parameter	Value	Source
Right Ascension	239.40	1
Declination	−30.14	1
Parallax, ϖ [mas]	68.1 ± 0.09	1
Distance, d [pc]	14.73 ± 0.02	1
Johnson V mag, m_V	5.65 ± 0.03	2
Gaia G mag, m_G	5.48 ± 0.01	1
$T_{\rm eff}$ [K]	5664 ± 130	3
[Fe/H] [dex]	−0.34 ± 0.04	3
Luminosity, $L_\star$ [$L_\odot$]	1.00 ± 0.04	This Work
$\nu_{\rm max}$ [μHz]	2810 ± 124	This Work
$\Delta\nu$ [μHz]	122.17 ± 1.62	This Work

2.4 Asteroseismology

The light curve was transformed to the frequency domain using the PBjam Power Spectral Density calculator (Nielsen et al. 2021). The resulting power spectrum is shown in Fig. 2, where the Gaussian-like power excess can be seen centered at ∼ 2700 μHz. This is consistent with the predicted power excess position based on scaling relations from the Asteroseismic Target List (Schofield et al. 2019; Hey et al. 2024), which predict a $\nu_{\rm max}$ between 2764 and 3344 μHz for this star, based on its radius and $T_{\rm eff}$.

2.4.1 Global Asteroseismic Parameters

There are two global asteroseismic parameters of interest: $\nu_{\rm max}$ and $\Delta\nu$. The frequency of maximum power, $\nu_{\rm max}$, is usually defined as the peak of the Gaussian-like envelope of oscillations in the power spectrum. The average frequency spacing between consecutive modes with the same angular degree, $\Delta\nu$, is easily estimated in solar-like oscillators, because pressure modes follow a semi-regular pattern. The frequencies (ν) of high radial order pressure modes of a given radial order (n_p) and angular degree ℓ are approximately given by

$$\nu_p(n_p, \ell) \approx \Delta\nu \left(n_p + \frac{\ell}{2} + \epsilon\right) - \delta\nu_{0\ell} \quad (1)$$

where ϵ is a phase term, and $\delta\nu_{0l}$ is a small frequency shift (Tassoul 1980; Scherrer et al. 1983).

Using the `estimate_deltanu` function in lightkurve, which applies an autocorrelation function, we estimated a value of $\Delta\nu$ = 123.38 μHz. To check the consistency of the features in the échelle diagram, we compare our resulting échelle diagram (Fig. 3) to that of a solar twin in the *Kepler* LEGACY sample (Lund et al. 2017), KIC 8424992. This sample is a gold-standard dataset of oscillating Sun-like dwarfs which were analysed using asteroseismology and *Kepler* data. KIC 8424992 is similar to ν^2 Lupi in terms of spectroscopic properties and $\nu_{\rm max}$. The comparison between the two échelle diagrams shows good agreement between ridges of oscillation modes. These are offset by the dimensionless asteroseismic phase term, ϵ (Tassoul 1980; Roxburgh & Vorontsov 2003). Following the $T_{\rm eff}$-ϵ relation found in *Kepler* stars by White et al. (2011a,b), we estimated the asteroseismic phase term of ν^2 Lupi to be $\epsilon \approx 0.4$.

To measure the global parameters, we used pySYD (Chontos et al. 2022), which estimates $\nu_{\rm max}$ from the smoothed power excess of a background corrected power spectrum. The best model used three Harvey-like components ($X = 3$) and a fixed white noise term. The final values were $\nu_{\rm max}$ = 2810 ± 124 μHz and $\Delta\nu$ = 122.17 ± 1.62 μHz.

2.4.2 Individual Frequencies

We employed the latest version of PBjam (Nielsen et al. 2025 in review; see Nielsen et al. 2021 for the first public release) to determine

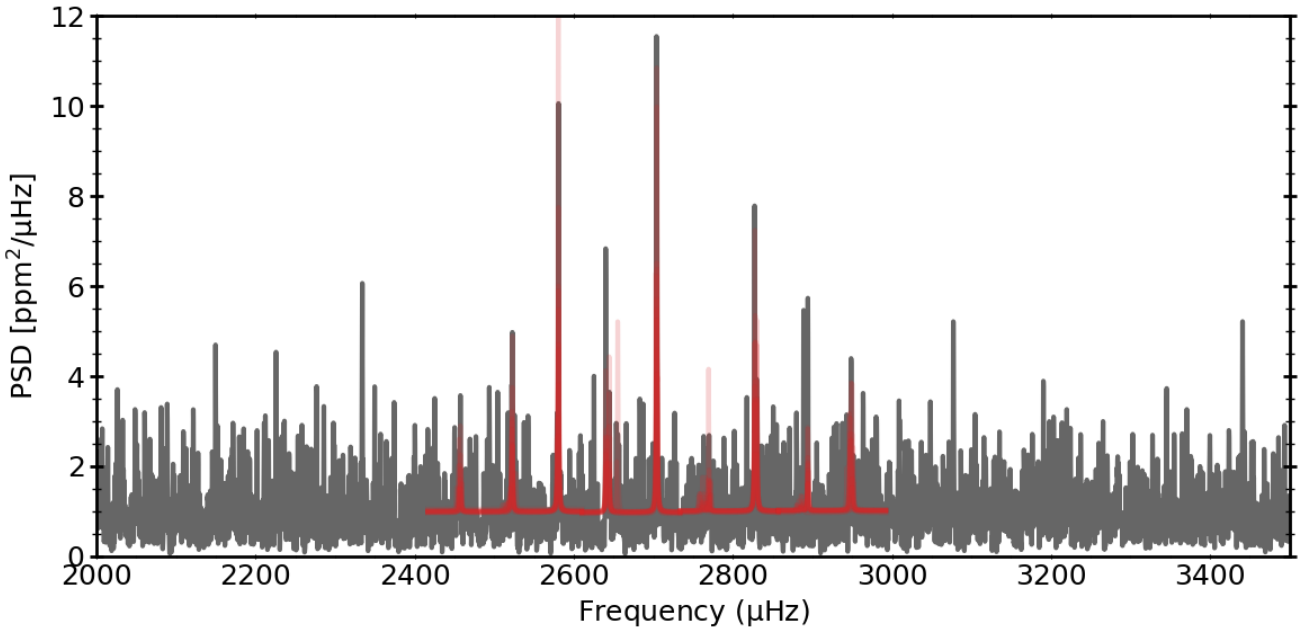

Figure 2. Power spectrum of ν^2 Lupi, with a clear power excess centered at $\sim$ 2700 μHz. The modelled oscillation envelope power spectrum from PBjam (Nielsen et al. 2021) is plotted on red atop the spectrum.

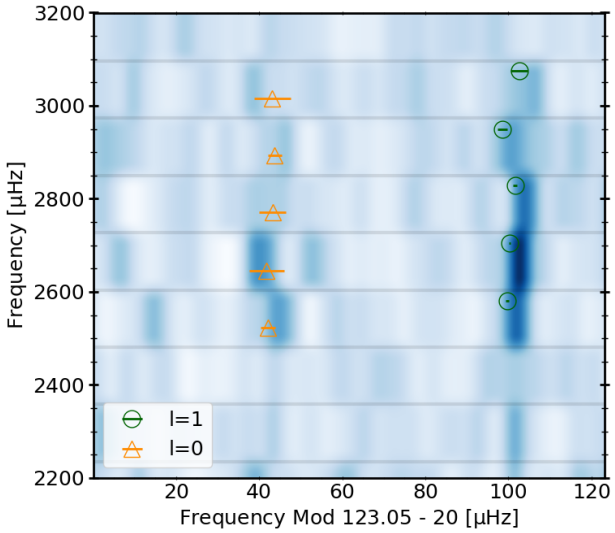

Figure 3. Échelle diagram of ν^2 Lupi. Sections of the power spectrum, sliced at the value of $\Delta\nu$ are stacked upon one another. The vertical ridges indicate the presence of regularly spaced oscillations. Frequencies at which oscillations are observed are indicated by overlaid symbols – green points for dipole modes, and orange for radial. Frequencies are shifted left by 20 μHz to improve visibility.

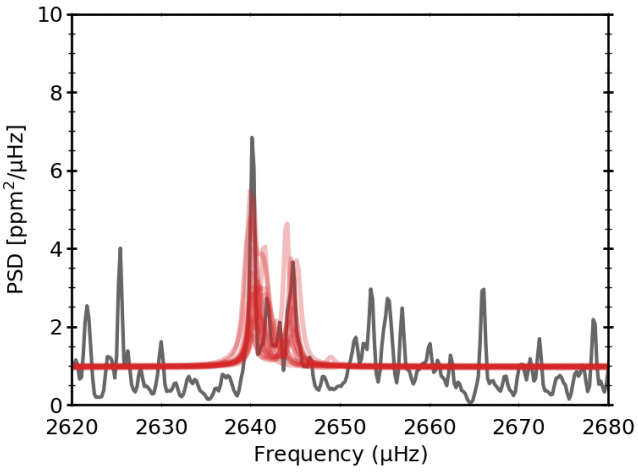

Figure 4. Power spectrum of ν^2 Lupi, zoomed to show the strongest example of a potential $\ell = 2$ mode in the spectrum, detected at $\sim$ 2648 μHz. Red lines show multiple draws from the posterior distribution of the power spectrum as sampled by the MCMC. The close-by $\ell = 0$ mode is visible at $\sim$ 2640 μHz.

the frequencies of the oscillation modes in the *TESS* data. PBjam is based on a Bayesian formalism which models the observed oscillation spectrum with a set of Lorentzian peaks, accounting for the $\ell = 2, 0$ mode pairs by utilizing prior information about the expected frequency structure and mode degeneracies from a set of observed *Kepler* oscillators. The parameter space is defined via Principal Component Analysis (PCA), which reduces the dimensionality of the data. The frequency, line width, and amplitude of each mode are identified, informed by both the asymptotic relation for p-modes (Eq. 1) and the characteristics of the observed power spectrum. Mode identification is then performed using a Markov Chain Monte Carlo (MCMC) method to explore this space, producing posterior distributions for each mode's parameters. Then, a spectrum model is iteratively fitted to the power spectrum, without the tight priors that are used in the

Table 3. Oscillation mode frequencies for ν^2 Lupi using the methods in Nielsen et al. (2021).

ℓ	Frequency [μHz]
1	2580.71 ± 0.44
0	2523.15 ± 1.69
1	2704.29 ± 0.21
0	2645.85 ± 4.22
1	2828.70 ± 0.48
0	2770.32 ± 3.30
1	2948.67 ± 1.14
0	2893.90 ± 1.68
1	3075.81 ± 2.07
0	3016.36 ± 4.44

mode identification stage. This allows for greater freedom in fitting, which is necessary because Eq. 1 is an approximation. This also provides mode frequency uncertainties.

We validated the mode identification by-eye, using the échelle diagram and a heavily smoothed version of the spectrum. Due to the low SNR, $\ell = 2$ modes were not easily identifiable visually, so this analysis included only $\ell = 0$ and $\ell = 1$ modes. Figure 4 shows the most prominent example of a $\ell = 0$ and $\ell = 2$ mode pair in the data, in grey, and as detected and modelled by PBjam, in red. More *TESS* sectors of data should allow for a more robust determination of these values, 2 of which will become available in April and May 2026.

As an independent confirmation of the PBjam analysis, mode frequencies were also determined following a third method, as outlined by Li et al. (2020). Lorentzian profiles were fit to the power spectrum, with a model which included background noise and granulation signals to isolate the oscillation modes. This method found frequencies that agree well with the PBjam output, but without significant detection of $\ell = 2$ peaks.

The frequencies of radial and diple modes adopted from PBjam, are listed in Table 3, which we use for stellar modelling. We note that $\ell = 0$ modes are less precise than the $\ell = 1$, due to the relative strength of the latter. This can be seen in Figure 2. Even near $\nu_{\rm max}$, $\ell = 0$ modes are relatively weak.

3 STELLAR MODELLING

3.1 Grid-Based Modelling

To determine precise stellar parameters, we employed four stellar models and fitting tools. This was done in order to compare the results of fitting the same observables with different methods, and generate estimates of systematic uncertainties for the estimated parameters.

3.1.1 BASTA

We used BASTA in conjunction with the dense grid of stellar models also used in Weeks et al. (2024). Briefly, this grid consists of ~ 6000 stellar evolutionary tracks computed with the Garching Stellar Evolution Code (Garstec, Weiss & Schlattl 2008). For equations of state, we used the OPAL group (Rogers et al. 1996; Rogers & Nayfonov 2002), and the Mihalas-Hummer-Däppen equation of state (Mihalas et al. 1988; Hummer & Mihalas 1988; Daeppen et al. 1988; Mihalas et al. 1990), and for opacities we used the OPAL opacities (Rogers & Iglesias 1992; Iglesias & Rogers 1996) as well as opacities from (Ferguson et al. 2005) at high and low temperatures, respectively. We used the NACRE nuclear reaction rates (Angulo et al. 1999) except for ^{14}N$(p,\gamma)^{15}$O and ^{12}C$(\alpha,\gamma)^{16}$O, for which

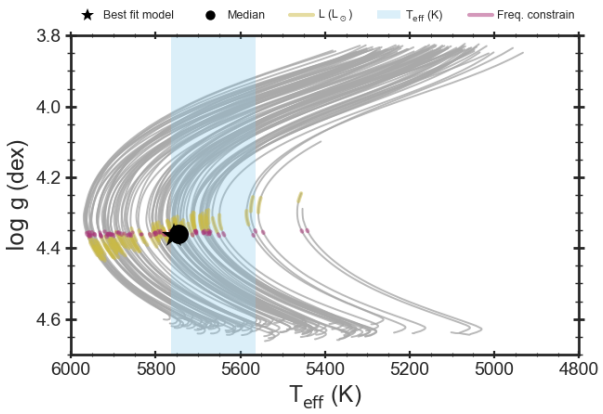

Figure 5. Kiel diagram showing several model tracks from Garstec, and the best-fit solutions for ν^2 Lupi, in $T_{\rm eff}$- $\log g$ space. The constraints from asteroseismology and effective temperature are shown in mauve and blue respectively, and the constraints from the `isoclassify`-determined luminosity are shown in yellow.

the rates from Formicola et al. (2004) and Hammer et al. (2005) were used. We choose to use the solar mixture from Asplund et al. (2009). The stellar grid spanned the following dimensions: stellar masses from 0.7–1.2 $M_\odot$, initial iron abundances from −1.0–0.6 dex, the initial alpha enhancement from −0.2–0.6, initial helium fraction from 0.24–0.32, the mixing length parameter, which parameterise the stellar convection (Böhm-Vitense 1958; Kippenhahn et al. 2012), from 1.6–2.0 with the solar calibrated value being $\alpha_{MLT_\odot} = 1.791$. We included the effects of atomic diffusion because it is crucial for obtaining accurate ages and masses of stars with $M_\star <$ 1.15 $M_\odot$ (Valle et al. 2014).

The sampling across the dimensions was neither random nor regularly Cartesian, but instead used Sobol quasi-random, low-discrepancy sequences (Sobol & Levithan 1976; Sobol 1977; Antonov & Saleev 1980; Fox 1986; Bratley & Fox 1988; Joe & Kuo 2003) in order to ensure evenly and effective sampling across the entire multi-dimensional volume of the grid. For each model along a track, we computed the theoretical asteroseismic mode frequencies using the Aarhus adiabatic oscillation package (adipls; Christensen-Dalsgaard 2008). Bolometric corrections of Hidalgo et al. (2018) were applied to calculate synthetic magnitudes, which were used alongside the 3D dustmaps from Green et al. (2019) to calculate the line-of-sight extinction. We folded in our prior expectation of the expected mass distribution of stars using the Salpeter initial mass function (Salpeter 1955) when computing the posterior distribution. Explicitly, our list of input observables for ν^2 Lupi was: effective temperature $T_{\rm eff}$, metallicity [Fe/H], the alpha enhancement [α/Fe], luminosity, and the set of individual mode frequencies of $\ell = 0, 1$ from PBjam. The position of the solution from this method with respect to models in $T_{\rm eff}$- $\log g$ space is shown in Fig. 5.

We also plot the observed frequencies and model frequencies in an échelle format, in Fig. 6.

3.1.2 MESA I

We also constructed a grid of stellar models with MESA (version r240301; Paxton et al. 2011, 2013, 2015, 2018, 2019; Jermyn et al. 2023). We adopted default MESA EOS and opacity tables compatible

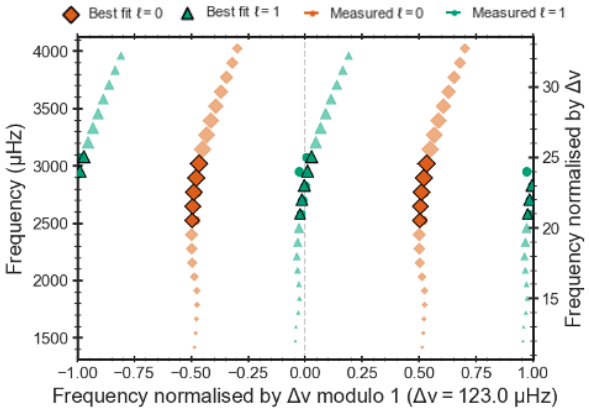

Figure 6. Échelle diagram showing the locations of the $\ell = 0$ (orange) and $\ell = 1$ (green) modes of ν^2 Lupi. Circles show the locations of the observed modes, and diamonds and triangles show the mode frequencies in the best-fit model determined by BASTA. We see the same ridges and frequencies as the observed frequencies plotted in 3.

with the solar abundance mixture of Asplund et al. (2009). We used the list of nuclear reactions from `pp_and_cno_extras.net`. Convection was treated with the mixing-length formulation of Henyey et al. (1965), and a moderate convective shell overshoot was applied with $f_{\rm ov,shell} = 0.0174$ (Herwig 2000). We used Eddington (1926)'s $T - \tau$ relation for modelling the atmospheric boundary condition, with opacity uniformly set to be consistent with the temperature and pressure at the base of the atmosphere.

We sampled a grid of stellar models in a four dimensional parameter space: stellar mass from 0.5 to 1.2 $M_\odot$, metallicity from -0.8 to 0.5 dex, mixing length parameter from 1.5 to 2.5 (with solar-calibrated value being 1.72), and initial helium fraction from 0.22 to 0.34. Approximately 60,000 evolutionary tracks were sampled using a Sobol sequence, with all models evolved to the end of the main sequence. The spatial structures were stored and and oscillation frequencies were computed using GYRE (version 7.1; Townsend & Teitler 2013).

We used the Bayesian fitting framework employed by Li et al. (2024) to determine stellar properties. To correct the surface effect of oscillation modes, we used the empirical cubic correction formula proposed by Ball & Gizon (2014). Typical procedures determine the free parameter, namely a_3 in the Ball & Gizon (2014) cubic correction formula, by minimizing the residuals between modelled and observed frequencies on a model-by-model basis. This can sometimes yield unrealistically large surface corrections as a result of improper match of the internal structure, therefore biasing posterior distributions. To mitigate this issue, we assumed that the amount of correction at $\nu_{\rm max}$ follows a normal distribution with a mean of 0.038 $\Delta\nu$ and a standard deviation of 0.020 $\Delta\nu$, based on best-fitting models. Based on this value, we calculated the cubic term a_3 and applied the correction to all oscillation modes.

3.1.3 MESA II

In the third grid-based modelling method, values and uncertainties were determined by the bootstrapping procedure described by Ong et al. (2021) using the main-sequence model grid from that work. This model grid was generated using MESA r12115, but with chemical compositions scaled relative to the solar abundances of Grevesse & Sauval (1998). The correction of Salaris et al. (1993) was applied to account for α-element abundances. A seismic penalty function was applied, which combines equally-weighted contributions from the surface-term correction of Ball & Gizon (2014, with coefficients fitted against only the radial modes, but with the cost function evaluated with respect to all corrected modes), and from the ϵ-matching procedure described by Roxburgh (2016). Unlike MESA I, no regularisation was applied to the coefficients of the free parameters in the surface-term correction.

Table 4. Physical Stellar Properties determined using the four methods detailed in 3.1

Method	Radius [$R_\star$]	Mass [$M_\star$]	Age [Gyr]
GARSTEC	$1.00^{+0.01}_{-0.01}$	$0.829^{+0.04}_{-0.03}$	$11.9^{+2.6}_{-1.6}$
MESA I	1.03 ± 0.04	0.89 ± 0.06	11.76 ± 2.43
MESA II	$1.04^{+0.03}_{-0.04}$	$0.84^{+0.03}_{-0.03}$	$10.91^{+1.38}_{-1.56}$
MESA III	1.00 ± 0.01	0.82 ± 0.06	12.64 ± 0.94

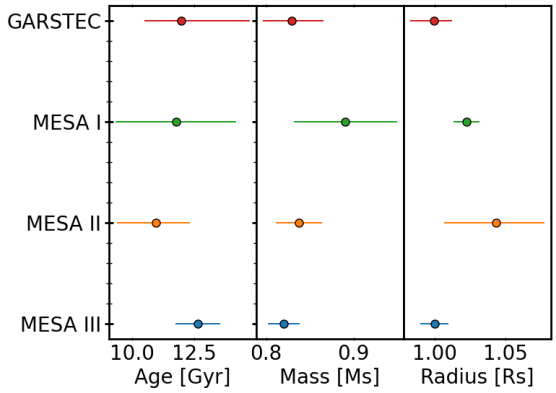

Figure 7. Comparison between values for mass, radius and age for ν^2 Lupi, using the same inputs, but different codes and stellar models, as noted on the y-axis. See section 3.1 for details.

3.1.4 MESA III

The final method employed the differential evolution algorithm implemented by Mier (2017) in order to find stellar parameters that best match both the spectroscopic and asteroseismic observables. The spectroscopic and seismic cost functions, as well as MESA (version r22.05.1) modelling choices employed in this method, were the same as by Lindsay et al. (2024), apart from an additional cost term. This was calculated from the difference between the asteroseismic surface term coefficient from Li et al. (2023) and that calculated directly from comparing the model mode frequencies to the observed frequencies (Ball & Gizon 2014). The initial mass ($0.8M_\odot \leq M_0 \leq 1.2M_\odot$), initial helium mass fraction ($0.24 \leq Y_0 \leq 0.27$), initial metallicity ($0.007 \leq Z_0 \leq 0.017$), and

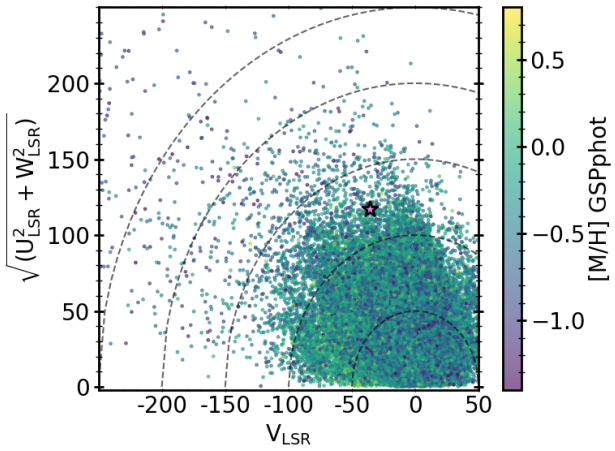

Figure 8. A Toomre diagram, depicting the kinematics of a sample of stars observed by *Gaia* DR3, with values of [Fe/H] < 1.4, Renormalised Unit Weight Error (RUWE < 1.4), and heliocentric distance $\lesssim$ 100 pc. The semicircles depict different total velocities (V_{tot}) and ν^2 Lupi is shown by the pink star.

convective mixing length ($1.75 \leq \alpha_{\rm mlt} \leq 1.85$) were varied for each evolutionary track. Solar calibration results in this formalism have offered a reference value of $\alpha_{\rm mlt}$ ~1.8. To account for the α-element enhancement of ν^2 Lupi ([α/Fe] = 0.15), the α-enhanced elemental mixtures and opacity tables were used in the model calculations. The errors of each model parameter were determined by taking the likelihood weighted standard deviation of each parameter.

3.1.5 Final Stellar Parameters

The median values for age, mass and radius from each modelling method are plotted in Fig. 7, along with their uncertainties. We use the values from BASTA as our final values (see Table 5), since its value for mass is the closest to the mean from all methods. We report random errors as calculated by BASTA, and systematic errors as the standard deviation of each parameter over the 4 methods. This gives a more accurate estimate of the true combined (measurement and systematic) uncertainties on these values, as recommended by Tayar et al. (2022) and Serenelli et al. (2017). It can be seen in Fig. 5 and Table 2 that using constraints from Gaia and asteroseismology prefer a slightly hotter $T_{\rm eff}$ than the spectroscopic value from previous literature, e.g. Delrez et al. (2021), but agrees more closely with photometric temperatures from e.g. Stassun et al. (2019). However, in general we find excellent agreement between the stellar parameters from BASTA and literature values for this star – see Table 5, now with the added precision from asteroseismology. We note that for age, the spread between methods is only ~ 1.7 Gyr, suggesting that the large random errors for age are conservative.

3.2 Thick Disk Membership

Determining the Galactic component to which each host star belongs is of interest when considering the effects of the star's birth environment on planet properties (Nielsen et al. 2023; Cabral et al. 2023). Understanding the population of exoplanets that orbit around thick and thin disk stars can shed light on planet demographics in the Galactic context (Bashi & Zucker 2019, 2022). In particular, Dai et al. (2021) found that stars with higher Galactic tangential velocity, often associated with the thick disk, have a lower occurrence rate of close-in super Earths and sub-Neptunes, compared to stars which orbit the centre of the Galaxy more slowly.

To identify the Galactic component to which ν^2 Lupi belongs, we inspected its kinematics. We first calculated the cylindrical Galactocentric velocities of the star (UVW) to be [105.22, 203.39, 45.58], using the Gaia parallax, proper motions in RA and DEC directions, and radial velocity. Fig. 8 shows a Toomre diagram – a plot showing the kinematics of stars in Galactic Velocity space. Sitting between the contours which depict $V_{\rm tot}$ = 100 and 200 km/s, ν^2 Lupi is kinematically consistent with the thick disk according to the definitions in Bashi & Zucker (2022). It is likely to be a member of the Galactic thick disk given that thin disk stars, with $V_{\rm tot} \lesssim$ 100 km/s, often have higher metallicities than those in the thick disk. This conclusion is supported by the [α/H] = 0.15 ±0.04 and [Fe/H] = -0.34 ±0.04 from Delrez et al. (2021), which are consistent with the Galactic thick disk (Vieira et al. 2022).

4 PLANET SYSTEM

4.1 Planet Parameters

With the new, precise asteroseismic values for this star, we recalculated parameters for the three planets in the ν^2 Lupi system. To re-calculate radius, we used the planet-to-star radius ratio ($R_p/R_\star$) from Delrez et al. (2021), alongside our newly calculated stellar parameters.

New planet masses were determined by using the values for radial velocity semi-amplitude (K) from Delrez et al. (2021), and

$$M_p \sin i = \frac{K}{K_0}\sqrt{1-e^2}\frac{M_\star}{M_\odot}\frac{2}{3}P^{\frac{1}{3}}, \quad (2)$$

as was applied, for example, by Fulton et al. (2018). Here, $M_\star$ is our new stellar mass, M_p is the planet mass, K the radial velocity semi-amplitude, i the inclination, e the eccentricity of the orbit, and P the orbital period.

These new parameters are shown in Fig. 9 and listed in Table 5. The parameters are slightly smaller than the values in Delrez et al. (2021) (3.6% in planet mass, and 5.4% in radius for the smallest planet), although still in agreement within uncertainties.

4.2 Radius Valley

It is useful to consider the location of the ν^2 Lupi planets in the context of the radius valley – a well-studied bimodality in the distribution of radii of small exoplanets, between 1 and 4 Earth radii (Fulton et al. 2017; Van Eylen et al. 2018). The dearth, which is exhibited at 1.5–2 $R_\oplus$, may be due to one or more of several planet formation and evolution processes. One branch of models postulates that atmospheric mass loss causes some of these planets to 'shrink' - from sub-Neptunes (above the gap), to super-Earths (below the gap) (Burn et al. 2024). This mass loss may be caused by photoevaporation from the host star (e.g. Lopez & Fortney 2013; Owen & Wu 2013; Rogers et al. 2021), or by core-powered mass loss (e.g. Ginzburg et al. 2018; Gupta & Schlichting 2019, 2020). Alternatively, the super-Earths may have formed after the disc has dissipated, thus prohibiting any significant atmosphere formation (Lopez & Rice 2018; Lee et al. 2022).

The location and slope of the valley as a function of orbital period was precisely determined by Van Eylen et al. (2018) using a population of 117 planets orbiting stars that were homogeneously and precisely characterised through asteroseismology. We added the

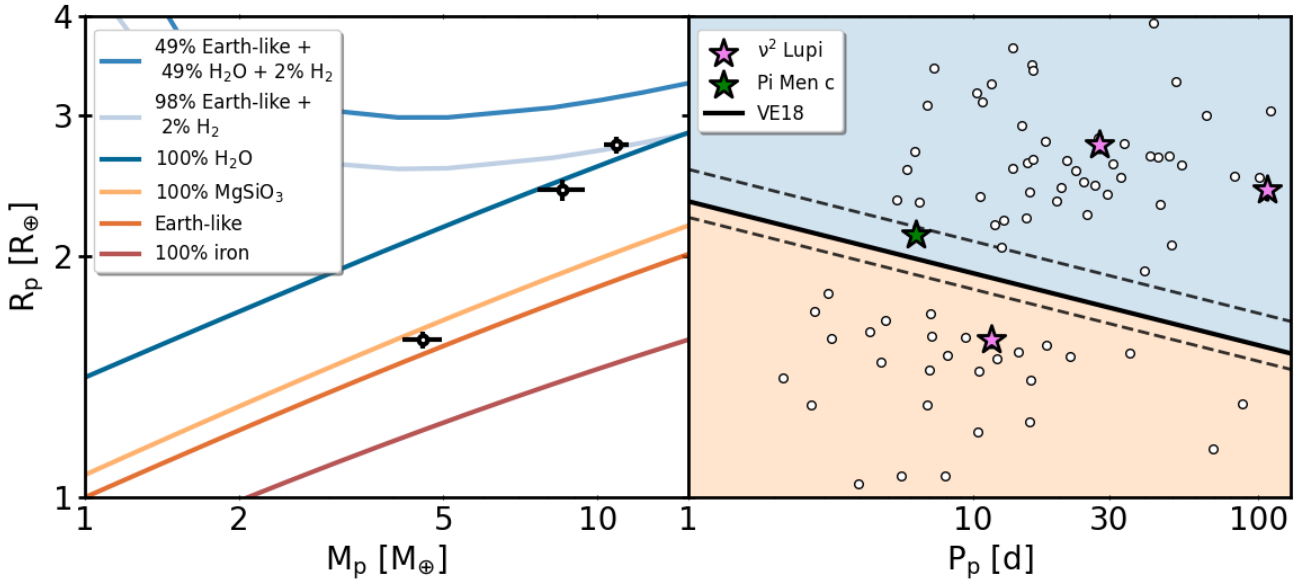

Figure 9. The three planets orbiting ν^2 Lupi. We plot recalculated values for mass and radius in the left panel. Compositional tracks are from Zeng et al. (2016). In the right hand panel, the updated asteroseismic radius valley is plotted. Planets from Van Eylen et al. (2018), which orbit stars which have been analysed with asteroseismology, are plotted as white circles. The radius valley determined from Van Eylen et al. (2018) is shown in the black line, with dashed grey line showing the upper and lower limits of the valley from the support vectors. The new asteroseismic radius of sub-Neptune π Men c, from Huber et al. (2022), is plotted as the green star. The recalculated values for ν^2 Lupi planets using asteroseismology in this work are plotted as the pink stars. Errors on both axes are smaller than the markers. As a visual aid, the area below the valley in orange is where we expect to see super-Earths. The blue-shaded area above is representative of sub-Neptunes.

three planets orbiting ν^2 Lupi to this asteroseismic radius valley sample, along with the planet orbiting the *TESS* asteroseismic host star, π Mensae (Huber et al. 2022). We have plotted this expanded sample in Fig. 9 (right panel). We observe that the new additions to the asteroseismic sample agree with the asteroseismic radius valley from Van Eylen et al. (2018). We also plotted the mass and radius of the three planets orbiting ν^2 Lupi, together with planet composition tracks from Zeng et al. (2016), in Fig 9 (left panel). From this figure, it can be seen that planet d, which is located below the radius valley, is consistent with a rocky composition, while planets b and c, which are located above the radius valley, are consistent with less dense, sub-Neptune like planets.

4.3 Planet Composition-Age connection

The connection between the properties of small, rocky exoplanets and their host stars provides important insights into planet formation (Bitsch & Battistini 2020; Mah & Bitsch 2023). Previous studies found rocky planets to have compositions which depend on the metallicity of their host star (Adibekyan et al. 2021), although when sub-Mercury sized planets are re-analysed, this trend became much weaker (Brinkman et al. 2024). Rocky planet density may also be linked to stellar age, with younger host stars (1–8 Gyr) forming rocky exoplanets with a greater diversity of compositions, whereas older stars host less dense planets (Weeks et al. 2024). This may be a result of Galactic chemical evolution – older stars are typically more alpha-enhanced and iron-poor.

We plotted ν^2 Lupi on a mass-radius diagram alongside members of the sample from Weeks et al. (2024) in Fig. 10. This shows planets in mass-radius space, compared to models of rocky planet composition from Zeng et al. (2016). Planets with compositions dominated by rocky materials in this plot are generally older, while the inverse is true for those which are more iron-rich. This may imply that more dense, iron-rich planets form preferentially around younger stars. In this sample, only four planets have asteroseismic host star ages, making any further such measurements important. The Earth-like planet in the ν^2 Lupi system is less dense than the Earth – estimated to be made of primarily rocky compounds, and with a low core mass fraction. This composition, in combination with the old age of the star, is in agreement with the trend observed by Weeks et al. (2024): older stars may host less dense rocky planets. Furthermore, the star is alpha-enhanced [α/Fe] $\sim$ 0.15 (Spitoni et al. 2020), which is also consistent with the expected trend.

5 CONCLUSIONS

We presented a re-characterisation of the bright planet host star, ν^2 Lupi, using analysis of individual frequencies of oscillation modes with asteroseismology. This target is the brightest host star for which oscillations have been detected in the *TESS* 20-second cadence data, with a TESS magnitude of 5.05 ±0.01, and the closest host star for which oscillations have been detected using photometry, at 14.73 ± 0.02 pc (Gaia Collaboration et al. 2016). We found $M_\star = 0.83^{+0.038}_{-0.030}$ (random error) ±0.04 (systematic error) $M_\odot$, and $R_\star = 1.00^{+0.013}_{-0.017}$ (random error) ±0.07 (systematic error) $R_\odot$. We also found it to be a likely member of the Galactic thick disk, with Galactocentric velocities of $UVW = [105, 203, 45]$ and an age of $11.9^{+2.6}_{-1.6}$

Parameter	Delrez et al. (2021)	This work
Star		
Mass [$M_\odot$]	$0.88^{+0.03}_{-0.03}$	$0.83^{+0.04}_{-0.03}$ (ran) ±0.07 (sys)
Radius [$R_\odot$]	1.05 ± 0.04	$1.00^{+0.01}_{-0.02}$ (ran) ±0.04 (sys)
Age [Gyr]	$11.7^{+2.1}_{-2.3}$	$11.9^{+2.6}_{-1.6}$ (ran) ±1.7 (sys)
Planet b		
Mass [$M_\oplus$]	4.72 ± 0.42	4.55 ± 0.40
Radius [$R_\oplus$]	1.66 ± 0.04	1.57 ± 0.04
Period [d]	$11.6^{+0.00008}_{-0.00013}$	
Planet c		
Mass [$M_\oplus$]	$11.24^{+0.65}_{-0.63}$	10.87 ± 0.62
Radius [$R_\oplus$]	$2.96^{+0.08}_{-0.07}$	2.75 ± 0.06
Period [d]	27.6 ± +0.001	
Planet d		
Mass [$M_\oplus$]	$8.82^{+0.93}_{-0.92}$	8.52 ± 0.90
Radius [$R_\oplus$]	$2.56^{+0.09}_{-0.08}$	2.42 ± 0.08
Period [d]	107.2 ± 0.1	

Table 5. Physical properties of the ν^2 Lupi system constituents, from Delrez et al. (2021) (left) and this work (right). Period is not recalculated in this study.

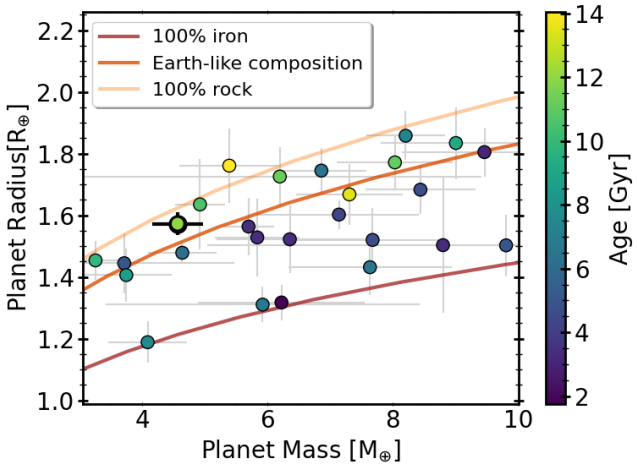

Figure 10. ν^2 Lupi's super-Earth (HD 136352-b), shown with a bold outline, in the context of other super-Earth planets with measured masses and radii. The sample and data are taken from Weeks et al. (2024). Planet composition models are again from Zeng et al. (2016). The highest, lighter orange line is the model of planetary composition of 100% $MgSiO_3$, i.e. 100% rocky mantle. The middle, darker orange line corresponds to Earth-like planets with 67.5% $MgSiO_3$, and 32.5% Fe. The lower darkest line represents planets composed of 100% Fe.

(randon error) ±1.7 (systematic error) Gyr, in agreement with previous studies. The precise asteroseismic parameters have allowed us to redetermine the planet parameters. Comparing these planets to other planets with asteroseismically determined stellar parameters, we showed that the asteroseismic radius valley remained empty. In addition, the precise asteroseismic age of the star supports the hypothesis that older stars host less dense rocky planets, and younger stars may be able to form planets with greater compositional diversity.

Asteroseismic characterisation of ν^2 Lupi provides precise parameters for a close, bright system with transiting exoplanets whose densities are well understood, as well as exquisite precision on its host star radius, mass and age. With three transiting planets located on both sides of the radius valley, one of which has a long 107-day orbital period, this system serves as a benchmark to better understand the formation of close-in transiting planets.

TESS will collect two more sectors of 20-second cadence data of this star – sectors 102 and 103, in April and May 2026. These will potentially enable detection of more oscillation modes, and thus a more tightly constrained stellar age. This may also offer insights into the spin-obit alignment of the system (Campante et al. 2016), as has been done with previous *Kepler* targets using asteroseismology (e.g. Huber et al. 2013a; Lund et al. 2014; Campante et al. 2016; Van Eylen et al. 2014). Finally, continued TESS 20-second cadence observations will provide asteroseismic ages for similar bright stars (e.g. Chontos et al. 2021; Hon et al. 2024), which may be found to host planets in future via direct imaging (Harada et al. 2024). These are crucial for the interpretation of possible atmospheric biosignatures that may be detected on planets orbiting these stars using future direct imaging missions, such as the Habitable Worlds Observatory (Bixel & Apai 2020). Such missions may also enable transmission spectroscopy for atmospheric studies of planets above and below the valley, in an exceptionally well characterised, thick-disk system.

ACKNOWLEDGEMENTS

A.W. would like to thank the Science and Technology Facilities Council (STFC) for funding support through a PhD studentship. V.V.E. and A.W. have been supported by UK's Science & Technology Facilities Council through the STFC grants ST/W001136/1 and ST/S000216/1. D.H. acknowledges support from the Alfred P. Sloan Foundation, the National Aeronautics and Space Administration (80NSSC22K0303, 80NSSC23K0434, 80NSSC23K0435), and the Australian Research Council (FT200100871). A.S. has been supported by funding from the European Research Council (ERC) under the European Union's Horizon 2020 research and innovation programme (CartographY; G. A. ID 804752). Funding for the Stellar Astrophysics Centre was provided by The Danish National Research Foundation (Grant agreement No. DNRF106). M.B.N acknowledges support from the UK Space Agency. J.M.J.O. acknowledges support from NASA through the NASA Hubble Fellowship grant HST-HF2-51517.001-A, awarded by STScI. STScI is operated by the Association of Universities for Research in Astronomy, Inc., under NASA contract NAS5-26555. T.R.B. acknowledges support from the Australian Research Council (FL220100117).

DATA AVAILABILITY

This research has made use of the NASA Exoplanet Archive, which is operated by the California Institute of Technology, under contract with the National Aeronautics and Space Administration under the Exoplanet Exploration Program. This work presents results from the European Space Agency (ESA) space mission Gaia. Gaia data are being processed by the Gaia Data Processing and Analysis Consortium (DPAC). Funding for the DPAC is provided by national institutions, in particular the institutions participating in the Gaia MultiLateral Agreement (MLA). The Gaia mission website is `https://www.cosmos.esa.int/Gaia`. The Gaia archive website is `https://archives.esac.esa.int/Gaia`.
This study makes use of `numpy` (Harris et al. 2020), `scipy` (Virtanen et al. 2020), `matplotlib` (Hunter 2007), `astropy` (Astropy Collaboration et al. 2013), `astroquery` (Ginsburg et al. 2019), and`BASTA` (Aguirre Børsen-Koch et al. 2022).

REFERENCES

Abazajian K. N., et al., 2009, ApJS, 182, 543
Adibekyan V., et al., 2021, Science, 374, 330
Aerts C., Christensen-Dalsgaard J., Kurtz D. W., 2010, Asteroseismology, doi:10.1007/978-1-4020-5803-5.
Aguirre Børsen-Koch V., et al., 2022, MNRAS, 509, 4344
Angulo C., et al., 1999, Nuclear Phys. A, 656, 3
Antonov I., Saleev V., 1980, USSR Computational Mathematics and Mathematical Physics, 19, 252
Asplund M., Grevesse N., Sauval A. J., Scott P., 2009, ARA&A, 47, 481
Astropy Collaboration et al., 2013, A&A, 558, A33
Ball W. H., Gizon L., 2014, A&A, 568, A123
Bashi D., Zucker S., 2019, AJ, 158, 61
Bashi D., Zucker S., 2022, MNRAS, 510, 3449
Basu S., 2016, Living Reviews in Solar Physics, 13, 2
Bean J. L., Raymond S. N., Owen J. E., 2021, Journal of Geophysical Research (Planets), 126, e06639
Bedding T. R., 2014, in Pallé P. L., Esteban C., eds, , Asteroseismology. p. 60, doi:10.48550/arXiv.1107.1723
Bedding T. R., Kjeldsen H., 2003, Publ. Astron. Soc. Australia, 20, 203
Berger T. A., Huber D., van Saders J. L., Gaidos E., Tayar J., Kraus A. L., 2020, AJ, 159, 280
Berger T. A., Schlieder J. E., Huber D., 2023, arXiv e-prints, p. arXiv:2301.11338
Bitsch B., Battistini C., 2020, A&A, 633, A10
Bixel A., Apai D., 2020, AJ, 896, 131
Böhm-Vitense E., 1958, Z. Astrophys., 46, 108
Boley K. M., et al., 2024, AJ, 168, 128
Bonomo A. S., et al., 2023, A&A, 677, A33
Bratley P., Fox B., 1988, ACM Transactions on Mathematical Software, 14, 88
Brinkman C. L., Polanski A. S., Huber D., Weiss L. M., Valencia D., Plotnykov M., 2024, AJ, 168, 281
Bruntt H., 2009, A&A, 506, 235
Bryant E. M., Bayliss D., Van Eylen V., 2023, MNRAS, 521, 3663
Burn R., Mordasini C., Mishra L., Haldemann J., Venturini J., Emsenhuber A., Henning T., 2024, Nature Astronomy, 8, 463
Cabral N., Guilbert-Lepoutre A., Bitsch B., Lagarde N., Diakite S., 2023, A&A, 673, A117
Campante T. L., et al., 2016, AJ, 819, 85
Campante T. L., et al., 2019, AJ, 885, 31
Chaplin W. J., Miglio A., 2013, ARA&A, 51, 353
Chaplin W. J., et al., 2011, Science, 332, 213
Chaplin W. J., et al., 2014, ApJS, 210, 1
Chen D.-C., et al., 2023, Proceedings of the National Academy of Science, 120, e2304179120
Chontos A., et al., 2021, AJ, 922, 229
Chontos A., Huber D., Sayeed M., Yamsiri P., 2022, The Journal of Open Source Software, 7, 3331
Christensen-Dalsgaard J., 2008, Ap&SS, 316, 113
Cloutier R., Menou K., 2020, AJ, 159, 211
Daeppen W., Mihalas D., Hummer D. G., Mihalas B. W., 1988, AJ, 332, 261
Dai Y.-Z., Liu H.-G., An D.-S., Zhou J.-L., 2021, AJ, 162, 46
Dai F., et al., 2023, AJ, 165, 33
David T. J., et al., 2021, AJ, 161, 265
Davies G. R., et al., 2016, MNRAS, 456, 2183
Delrez L., et al., 2021, Nature Astronomy, 5, 775
DiTomasso V., López-Morales M., Peacock S., Malavolta L., Kirk J., Stevenson K. B., Fu G., Lustig-Yaeger J., 2025, AJ, 979, 214
Eddington A. S., 1926, The Internal Constitution of the Stars
Ehrenreich D., et al., 2023, A&A, 671, A154
Ferguson J. W., Alexander D. R., Allard F., Barman T., Bodnarik J. G., Hauschildt P. H., Heffner-Wong A., Tamanai A., 2005, AJ, 623, 585
Fischer D. A., Valenti J., 2005, AJ, 622, 1102
Formicola A., et al., 2004, Physics Letters B, 591, 61
Fox B., 1986, ACM Transactions on Mathematical Software, 12, 362
Fulton B. J., et al., 2017, AJ, 154, 109
Fulton B. J., Petigura E. A., Blunt S., Sinukoff E., 2018, PASP, 130, 044504
Gaia Collaboration et al., 2016, A&A, 595, A1
Gaia Collaboration et al., 2021, A&A, 649, A1
Gan T., et al., 2023, AJ, 165, 17
García R. A., Ballot J., 2019, Living Reviews in Solar Physics, 16, 4
Ginsburg A., et al., 2019, AJ, 157, 98
Ginzburg S., Schlichting H. E., Sari R., 2018, MNRAS, 476, 759
Gonzalez G., 1997, MNRAS, 285, 403
Green G. M., Schlafly E., Zucker C., Speagle J. S., Finkbeiner D., 2019, AJ, 887, 93
Grevesse N., Sauval A. J., 1998, Space Sci. Rev., 85, 161
Grunblatt S. K., Huber D., Gaidos E., Hon M., Zinn J. C., Stello D., 2019, AJ, 158, 227
Guerrero N. M., et al., 2021, ApJS, 254, 39
Guggenberger E., Hekker S., Basu S., Bellinger E., 2016, MNRAS, 460, 4277
Gupta A., Schlichting H. E., 2019, MNRAS, 487, 24
Gupta A., Schlichting H. E., 2020, MNRAS, 493, 792
Hammer J., et al., 2005, Nuclear Physics A, 758, 363
Harada C. K., Dressing C. D., Kane S. R., Ardestani B. A., 2024, ApJS, 272, 30
Harris C. R., et al., 2020, Nature, 585, 357
Henyey L., Vardya M. S., Bodenheimer P., 1965, AJ, 142, 841
Herwig F., 2000, A&A, 360, 952
Hey D., Huber D., Ong J., Stello D., Foreman-Mackey D., 2024, arXiv e-prints, p. arXiv:2403.02489
Hidalgo S. L., et al., 2018, The Astrophysical Journal, 856, 125
Ho C. S. K., Rogers J. G., Van Eylen V., Owen J. E., Schlichting H. E., 2024, MNRAS, 531, 3698
Hon M., et al., 2024, AJ, 975, 147
Howard A. W., et al., 2012, ApJS, 201, 15
Huber D., et al., 2013a, Science, 342, 331
Huber D., et al., 2013b, AJ, 767, 127
Huber D., et al., 2017, AJ, 844, 102
Huber D., et al., 2019, AJ, 157, 245
Huber D., et al., 2022, AJ, 163, 79
Hummer D. G., Mihalas D., 1988, AJ, 331, 794
Hunter J. D., 2007, Computing in Science & Engineering, 9, 90
Iglesias C. A., Rogers F. J., 1996, AJ, 464, 943
Jenkins J. M., et al., 2016, in Chiozzi G., Guzman J. C., eds, Society of Photo-Optical Instrumentation Engineers (SPIE) Conference Series Vol. 9913, Software and Cyberinfrastructure for Astronomy IV. p. 99133E, doi:10.1117/12.2233418
Jermyn A. S., et al., 2023, ApJS, 265, 15
Jiang C., et al., 2023, AJ, 945, 20
Joe S., Kuo F., 2003, ACM Transactions on Mathematical Software, 29, 49
Kane S. R., et al., 2020, AJ, 160, 129
Kayhan C., Yıldız M., Çelik Orhan Z., 2019, MNRAS, 490, 1509

Kippenhahn R., Weigert A., Weiss A., 2012, Stellar Structure and Evolution. Springer Berlin, doi:10.1007/978-3-642-30304-3
Kjeldsen H., Bedding T. R., 1995, A&A, 293, 87
Kjeldsen H., Bedding T. R., 2011, A&A, 529, L8
Lebreton Y., Goupil M. J., Montalbán J., 2014, in Lebreton Y., Valls-Gabaud D., Charbonnel C., eds, EAS Publications Series Vol. 65, EAS Publications Series. pp 177–223 (arXiv:1410.5337), doi:10.1051/eas/1465005
Lee E. J., Karalis A., Thorngren D. P., 2022, AJ, 941, 186
Li Y., Bedding T. R., Li T., Bi S., Stello D., Zhou Y., White T. R., 2020, MNRAS, 495, 2363
Li Y., et al., 2023, MNRAS, 523, 916
Li Y., et al., 2024, AJ, 974, 77
Lindsay C. J., Ong J. M. J., Basu S., 2024, AJ, 965, 171
Lopez E. D., Fortney J. J., 2013, AJ, 776, 2
Lopez E. D., Rice K., 2018, MNRAS, 479, 5303
Lund M. N., et al., 2014, A&A, 570, A54
Lund M. N., et al., 2017, AJ, 835, 172
Lundkvist M. S., et al., 2016, Nature Communications, 7, 11201
Lundkvist M. S., Huber D., Silva Aguirre V., Chaplin W. J., 2018, arXiv e-prints, p. arXiv:1804.02214
Magrini L., et al., 2022, A&A, 663, A161
Mah J., Bitsch B., 2023, A&A, 673, A17
Ment K., Charbonneau D., 2023, AJ, 165, 265
Mier P. R., 2017, pablormier/yabox: v1.0.3, doi:10.5281/zenodo.848679
Mihalas D., Dappen W., Hummer D. G., 1988, AJ, 331, 815
Mihalas D., Hummer D. G., Mihalas B. W., Daeppen W., 1990, AJ, 350, 300
Miyazaki S., Masuda K., 2023, AJ, 166, 209
Nielsen M. B., et al., 2020, A&A, 641, A25
Nielsen M. B., et al., 2021, AJ, 161, 62
Nielsen J., Gent M. R., Bergemann M., Eitner P., Johansen A., 2023, arXiv e-prints, p. arXiv:2308.15504
Ong J. M. J., Basu S., McKeever J. M., 2021, AJ, 906, 54
Owen J. E., 2019, Annual Review of Earth and Planetary Sciences, 47, 67
Owen J. E., Wu Y., 2013, AJ, 775, 105
Owen J. E., Wu Y., 2017, AJ, 847, 29
Paxton B., Bildsten L., Dotter A., Herwig F., Lesaffre P., Timmes F., 2011, ApJS, 192, 3
Paxton B., et al., 2013, ApJS, 208, 4
Paxton B., et al., 2015, ApJS, 220, 15
Paxton B., et al., 2018, ApJS, 234, 34
Paxton B., et al., 2019, ApJS, 243, 10
Ricker G. R., et al., 2015, Journal of Astronomical Telescopes, Instruments, and Systems, 1, 014003
Rogers F. J., Iglesias C. A., 1992, ApJS, 79, 507
Rogers F. J., Nayfonov A., 2002, AJ, 576, 1064
Rogers J. G., Owen J. E., 2021, MNRAS, 503, 1526
Rogers F. J., Swenson F. J., Iglesias C. A., 1996, AJ, 456, 902
Rogers J. G., Gupta A., Owen J. E., Schlichting H. E., 2021, MNRAS, 508, 5886
Roxburgh I. W., 2016, A&A, 585, A63
Roxburgh I. W., Vorontsov S. V., 2003, A&A, 411, 215
Salaris M., Chieffi A., Straniero O., 1993, AJ, 414, 580
Salpeter E. E., 1955, AJ, 121, 161
Sayeed M., Angus R., Berger T. A., Lu Y., Christiansen J. L., Foreman-Mackey D., Ness M. K., 2025, AJ, 169, 112
Scherrer P. H., Wilcox J. M., Christensen-Dalsgaard J., Gough D. O., 1983, Sol. Phys., 82, 75
Schofield M., et al., 2019, ApJS, 241, 12
Serenelli A., et al., 2017, ApJS, 233, 23
Silva Aguirre V., et al., 2015, MNRAS, 452, 2127
Sobol I., 1977, USSR Computational Mathematics and Mathematical Physics, 16, 236
Sobol I., Levithan Y., 1976, IPM Akademii Nauk SSSR
Sousa S. G., et al., 2008, A&A, 487, 373
Spitoni E., Verma K., Silva Aguirre V., Calura F., 2020, A&A, 635, A58
Stassun K. G., et al., 2019, AJ, 158, 138
Swastik C., Banyal R. K., Narang M., Unni A., Banerjee B., Manoj P., Sivarani T., 2023, AJ, 166, 91
Tassoul M., 1980, ApJS, 43, 469
Tayar J., Claytor Z. R., Huber D., van Saders J., 2022, AJ, 927, 31
Townsend R. H. D., Teitler S. A., 2013, MNRAS, 435, 3406
Tsantaki M., et al., 2025, arXiv e-prints, p. arXiv:2502.20950
Udry S., et al., 2019, A&A, 622, A37
Valle G., Dell'Omodarme M., Prada Moroni P. G., Degl'Innocenti S., 2014, A&A, 567, A133
Van Eylen V., et al., 2014, AJ, 782, 14
Van Eylen V., Agentoft C., Lundkvist M. S., Kjeldsen H., Owen J. E., Fulton B. J., Petigura E., Snellen I., 2018, MNRAS, 479, 4786
Venturini J., Guilera O. M., Haldemann J., Ronco M. P., Mordasini C., 2020, A&A, 643, L1
Vieira K., Carraro G., Korchagin V., Lutsenko A., Girard T. M., van Altena W., 2022, AJ, 932, 28
Virtanen P., et al., 2020, Nature Methods, 17, 261
Weeks A., et al., 2024, arXiv e-prints, p. arXiv:2411.17358
Weiss A., Schlattl H., 2008, Ap&SS, 316, 99
White T. R., et al., 2011a, ApJ, 742, L3
White T. R., Bedding T. R., Stello D., Christensen-Dalsgaard J., Huber D., Kjeldsen H., 2011b, AJ, 743, 161
Yıldız M., çelik Orhan Z., Kayhan C., 2019, MNRAS, 489, 1753
Zeng L., Sasselov D. D., Jacobsen S. B., 2016, AJ, 819, 127

This paper has been typeset from a TEX/LATEX file prepared by the author.